ACS OMEGA

http://pubs.acs.org/journal/acsodf

Article

Intensification Effect of a Multi-Jet Structure on a Multiphase Flow and Desulfurization Process in a Fluidized Bed

Shuai Wang, Feng Wu,* Bei bei Di, Yuan Yan, and Yang chao Tang

Cite This: *ACS Omega* 2023, 8, 5861−5876

Read Online

ACCESS | Metrics & More | Article Recommendations

ABSTRACT: The introduction of a multi-jet structure at the bottom and middle of a fluidized bed can intensify the interphase mixing and improve desulfurization efficiency. The computational fluid dynamics were used to study the gas−liquid−solid flow in a bottom multi-jet fluidized bed and middle multi-jet fluidized bed (BMJFB and MMJFB). It was found that for the gas−liquid−solid interphase mixing, the intensification effect of introducing the multi-jet structure in the middle of the bed is more obvious than that in the bottom. The effect of the water spray volume flow rate on the MMJFB was examined under the same conditions. The results showed that with the increase of the water flow rate, the gas−liquid−solid interphase mixing and desulfurization process are promoted in the MMJFB, and its desulfurization efficiency reaches 68.2%. The effects of the width and number of multi-jet structures on the MMJFB were also investigated. The results show that when the jet width is 20 mm and the number of jets is four, the gas−liquid−solid three-phase is uniformly mixed and the desulfurization efficiency of the MMJFB equals 69.3%, which is 18.5% higher than that of the conventional fluidized bed.

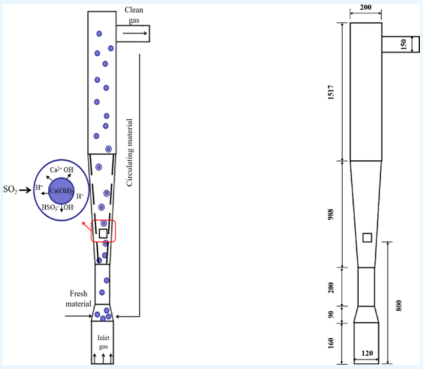

1. INTRODUCTION

In recent years, China has increasingly advocated the use of clean energy,[1,2] such as solar energy, wind energy, nuclear energy, etc., to protect the environment and improve air quality. However, China's resource structure of rich coal, lack of oil, and less gas determines the main position of coal in the energy consumption structure.[3] At present, coal is still the main energy for power generation, accounting for more than 36% of the total global power generation. Moreover, large-scale production technologies such as coal-to-oil have improved and extended the dominant position of coal.[4] Therefore, in fact, the dominant position of coal in China has not been shaken.[5] Coal is widely used in the mountainous areas of Southwest China and Northern China in winter. The massive use of coal has led to the increasingly prominent pollution of sulfur dioxide in the air. In addition, immature desulfurization technology will cause air pollution and pose a serious threat to environmental protection. Acid rain pollution has appeared in some areas in the south. In addition, the scope of acid rain pollution is also expanding. Therefore, how to effectively reduce SO_2 in flue gas emissions is very necessary.[6−10]

At present, hundreds of sulfur dioxide emission control technologies have been developed and applied all over the world. These technologies can be generally divided into three categories according to their position in the combustion process, namely, desulfurization before combustion (fuel desulfurization),[11] desulfurization during combustion (furnace desulfurization),[12] and desulfurization after combustion (flue gas desulfurization).[13,14] There are three ways of flue gas desulfurization, namely, dry desulfurization, semi-dry desulfurization, and wet desulfurization.[15−17] Semi-dry circulating fluidized bed flue gas desulfurization (CFB-FGD) combines the characteristics of dry desulfurization and wet desulfurization. It has the advantages of high desulfurization efficiency, low equipment cost, and small corrosion to equipment[16] and shows great application potential.

Ma et al.[18−20] applied binary mixed particles to low-temperature desulfurization and developed a new semi-dry FGD process. Limestone was used to replace the desulfurizer hydrated lime. The effects of the Ca/S molar ratio, the particle diameter of SO_2 absorbents, and near saturation temperature on the efficiency of semi-dry FGD were studied. Based on the magnetic fluidized bed, Zhang et al.[21,22] adopted a new semi-dry FGD technology. The research shows that the addition of an external magnetic field can loosen the surface of ferromagnetic particles, reduce the mass transfer resistance of droplets, increase the oxidation of S, and improve the desulfurization efficiency. Tsinghua University has also conducted a series of studies on semi-dry FGD in CFB, including the effects of desulfurizers,[23] operating conditions,[24−26] and CFB structure[27] on the

Received: November 30, 2022
Accepted: January 23, 2023
Published: February 3, 2023

ACS Publications

© 2023 The Authors. Published by American Chemical Society

Table 1. Governing Equations of the Multiphase Flow Model

mass conservation equation		
gas	$\frac{\partial}{\partial t}(\alpha_g\rho_g) + \nabla\cdot(\alpha_g\rho_g v_g) = -\dot{m}_{gl}$	(T1-1)
solid	$\frac{\partial}{\partial t}(\alpha_s\rho_s) + \nabla\cdot(\alpha_s\rho_s v_s) = -\dot{m}_{sl}$	(T1-2)
liquid	$\frac{\partial}{\partial t}(\alpha_s\rho_s) + \nabla\cdot(\alpha_s\rho_s v_s) = \dot{m}_{gl} + \dot{m}_{sl}$	(T1-3)
momentum conservation equation[33]		
gas	$\frac{\partial}{\partial t}(\alpha_g\rho_g v_g) + \nabla\cdot(\alpha_g\rho_g v_g v_g) = -\alpha_g\nabla P_g + \alpha_g\rho_g g + \nabla\cdot(\alpha_g\tau_g) + \beta_{gs}(v_s - v_g) + \beta_{gl}(v_l - v_g) + \beta_{gp}(v_p - v_g) - \dot{m}_{gl}v_{gl}$	(T1-4)
solid	$\frac{\partial}{\partial t}(\alpha_s\rho_s v_s) + \nabla\cdot(\alpha_s\rho_s v_s v_s) = -\alpha_s\nabla P_g - \nabla P_s + \nabla\cdot(\alpha_s\tau_s) + \alpha_s\rho_s g + \beta_{gs}(v_g - v_s) + \beta_{ls}(v_l - v_s) - \dot{m}_{sl}v_{sl}$	(T1-5)
liquid	$\frac{\partial}{\partial t}(\alpha_l\rho_l v_l) + \nabla\cdot(\alpha_l\rho_l v_l v_l) = -\alpha_l\nabla P_l + \alpha_l\rho_l g + \nabla\cdot(\alpha_l\tau_l) + \beta_{gl}(v_g - v_l) + \beta_{ls}(v_s - v_l) + \dot{m}_{gl}v_{gl} + \dot{m}_{sl}v_{sl}$	(T1-6)
energy conservation equation (q = g, s, l)		
	$\frac{\partial}{\partial t}(\alpha_q\rho_q h_q) + \nabla\cdot(\alpha_q\rho_q v_q h_q) = -\alpha_q\frac{\partial P_q}{\partial t} + \tau\colon\nabla v_q - \nabla q_q + \sum_{s=1}^{n}(Q_{sq} + \dot{m}_{sq}h_{sq} - \dot{m}_{qs}h_{qs})$	(T1-7)
	$h_q = \int_{T_{ref}}^{T} C_{P,w}\, d_T$	(T1-8)
where T_{ref} = 298.15 K		

desulfurization process. Tang et al.[28] studied how to increase the desulfurization efficiency by adding a bypass pipe next to the CFB. In order to further improve the desulfurization efficiency, more in-depth research on CFB-FGD should be carried out to meet the national standards and specifications.

With the closer integration of computer technology and the chemical industry, numerical simulation can be more widely used in fluidization research. Due to the restrictive problems of experimental equipment and funds and because some subtle processes in the experimental process are difficult to observe, computer simulation and experiments can be combined and complemented to understand the flow characteristics of the fluid in a fluidized bed more deeply. Because the multiphase flow and water vaporization process have a great impact on the desulfurization process, Du et al.[29] found that the three-dimensional results were more accurate than the two-dimensional results by numerically simulating the multiphase flow and water evaporation process in a spouted bed. The simulations also showed that the gas velocity, liquid temperature, and gas humidity all affect the water evaporation process. Based on fluid dynamics, Wang et al.[30] studied the semi-dry FGD process of circulating fluidized bed reactors by using the Euler−Euler model and the O−S resistance model and discussed the influence of operating parameters on desulfurization efficiency. It is found that the volume fraction of water in the particle phase plays an important role in the desulfurization process, so the water spray volume flow rate is the most significant parameter affecting the desulfurization effect, followed by the mass flow of circulating particles. Cai et al.[31] slightly changed the structure of the fluidized bed on the basis of Wang,[30] assuming that each droplet is only wrapped with one desulfurization particle for dissolution and mass transfer, simplified the desulfurization model based on the two-film theory (TFT), and simulated the effects of sulfur dioxide inlet concentration (A), inlet gas flow rate (B), circulating particle mass flow rate (C), and water spray volume flow rate (D) on the desulfurization effect of the circulating fluidized bed. The simulation results are combined with response surface method analysis to determine the optimal parameter conditions. In addition, the results show that the water spray volume flow rate has the greatest impact on the desulfurization effect. The desulfurization simulation is carried out under the best parameter conditions, and the results show that the desulfurization efficiency has been greatly improved.

To sum up, desulfurization experiments or simulations are carried out on fluidized beds with external magnetic fields, fluidized beds with external bypass tubes, or spouted beds with multi-jet, but there is almost no desulfurization model with multi-jet in the fluidized bed. Whether the inclusion of a multi-jet structure in a fluidized bed is similar to a spouted bed can facilitate the gas−liquid−solid mixing and desulfurization process. Therefore, in this paper, based on the desulfurization model established by Cai's[31] conventional fluidized bed and TFT, multi-jet was added to the bottom and middle of the conventional fluidized bed, respectively, and two new models, bottom multi-jet fluidized bed (BMJFB) and middle multi-jet fluidized bed (MMJFB), are constructed. The two new models are numerically simulated and compared with the traditional fluidized bed. According to Cai's[31] research, it is found that the volume flow rate of water spray has a significant impact on the desulfurization process. Therefore, the MMJFB desulfurization process with different water spray volume flow rates will also be numerically simulated. Thus, it provides a theoretical basis for the desulfurization process of MJFB.

2. MATERIALS AND METHODS

In this paper, numerical simulations were performed using FLUENT 15.0 computational fluid dynamics (CFD) software. The Euler−Euler model is used to simulate the multiphase flow process and desulfurization process.

2.1. Multiphase Flow Model. The system includes gas, liquid, and solid three phases, and the gas−liquid−solid three phases are considered continuous phases. β represents the interface momentum transfer coefficient, The Gidaspow model is used to depict the drag force between sorbent and gas,[32] the

https://doi.org/10.1021/acsomega.2c07658
ACS Omega 2023, 8, 5861−5876

Table 2. Constitutive Relations of the Multiphase Flow Model

component transport equation ($i = H_2O, SO_2, O_2$ in the gas phase)

$$\frac{\partial}{\partial t}(\alpha_i\rho_i Y_{j,i}) + \nabla(\alpha_i\rho_i v_1 Y_{j,i}) = \nabla\alpha_i J_{j,i} + R_{j,i}\alpha_i \quad \text{(T2-1)}$$

granular temperature conservation equation

$$\frac{3}{2}\left[\frac{\partial}{\partial t}(\alpha_s\rho_s\theta_s) + \nabla\cdot(\alpha_s\rho_s\theta_s v_s)\right] = (-\nabla p_s I + \alpha_s\tau_s): \nabla v_s + \nabla\cdot(k_{\theta_s}\nabla\theta_s) - \gamma_{\theta_s} - 3\beta_{gs}\theta_s \quad \text{(T2-2)}$$

turbulent kinetic energy equation of the gas phase

$$\frac{\partial}{\partial t}(\alpha_g\rho_g k_g) + \nabla\cdot(\alpha_g\rho_g v_g k_g) = \nabla\cdot\left(\alpha_g\frac{\mu_t}{\sigma_k}\nabla k_g\right) + \alpha_g G_k - \alpha_g\rho_g\alpha_g + \alpha_g\rho_g\Pi_{k_q} \quad \text{(T2-3)}$$

energy dissipation rate equation of the gas phase

$$\frac{\partial}{\partial t}(\alpha_g\rho_g\alpha_g) + \nabla(\alpha_g\rho_g v_g\alpha_g) = \nabla\cdot\left(\alpha_g\frac{\mu_t}{\sigma_\varepsilon}\nabla\alpha_g\right) + \alpha_g\frac{\alpha_g}{k_g}(C_{1\varepsilon}G_k - C_{2\varepsilon}\rho_g\alpha_g) + \alpha_g\rho_g\Pi_{k_q} \quad \text{(T2-4)}$$

stress tensor

$$\tau_g = \mu_g\left[\nabla v_g + (\nabla v_g)^T - \frac{2}{3}(\nabla v_g)I\right] \quad \text{(T2-5)}$$

$$\tau_s = \mu_s(\nabla v_s + \nabla v_s^T) + \left(\lambda_s - \frac{2}{3}\mu_s\right)\nabla v_s I \quad \text{(T2-6)}$$

$$\tau_l = \mu_l\left[\nabla v_l + (\nabla v_l)^T - \frac{2}{3}(\nabla v_l)I\right] \quad \text{(T2-7)}$$

solid pressure

$$p_s = \alpha_s\rho_s\theta_s + 2\rho_s(1 + e_s)\alpha_s^2 g_0\theta_s \quad \text{(T2-8)}$$

solid shear viscosity[34]

$$\mu_s = \mu_{s,\,col} + \mu_{s,\,kin} + \mu_{s,\,fr} \quad \text{(T2-9)}$$

$$\mu_{s,col} = \frac{4}{5}\alpha_s^2\rho_s d_s g_0(1 + e_s)\sqrt{\frac{\theta_s}{\pi}} \quad \text{(T2-10)}$$

$$\mu_{s,kin} = \frac{10\rho_s d_s\sqrt{\pi\theta_s}}{96(1 + e_s)\alpha_s g_0}\left[1 + \frac{4}{5}\alpha_s g_0(1 + e_s)\right]^2\alpha_s \quad \text{(T2-11)}$$

frictional viscosity[35]

$$\mu_{s,fr} = \frac{p_s\sin(\theta)}{2\sqrt{I_{2D}}} \quad \text{(T2-12)}$$

solid radial distribution function

$$g_0 = [1 - (\alpha_s/\alpha_{s,\,max})^{1/3}]^{-1} \quad \text{(T2-13)}$$

solid bulk viscosity

$$\lambda_s = \frac{4}{3}\alpha_s\rho_s g_0(1 + e_s)\sqrt{\frac{\theta_s}{\pi}} \quad \text{(T2-14)}$$

collisional energy dissipation

$$\gamma = \frac{12(1 - e_s^2)g_0}{d_s\sqrt{\pi}}\rho_s\alpha_s^2\theta_s^{3/2} \quad \text{(T2-15)}$$

diffusion coefficient of granular energy[34]

$$k_s = \frac{150 d_s\rho_s\sqrt{\theta_s\pi}}{384(1 + e_s)g_0}\left[1 + \frac{6}{5}\alpha_s g_0(1 + e_s)\right]^2 + 2\rho_s d_s\alpha_s^2 g_0(1 + e_s)\sqrt{\frac{\theta_s}{\pi}} \quad \text{(T2-16)}$$

interface momentum transfer coefficient[36−38]

$$\beta_{Gidaspow} = 150\frac{\alpha_s^2\mu_g}{\alpha_g d_s^2} + 1.75\frac{\alpha_s\rho_g|v_g - v_s|}{d_s} \quad \text{(T2-17)}$$

$$\beta_{Symmetric} = \frac{\alpha_g(\alpha_l\rho_l + \alpha_g\rho_g)}{\tau_{gl}}\cdot\frac{C_D Re}{24} \quad \text{(T2-18)}$$

$$\beta_{Wen\text{-}Yu} = \frac{3}{4}C_D\frac{\alpha_s\alpha_g\rho_g|v_s - v_g|}{d_s}\alpha_g^{-2.7} \quad \text{(T2-19)}$$

$$C_D = \begin{cases} \dfrac{24}{\alpha_g Re}(1 + 0.15(\alpha_g Re)^{0.687}) & Re < 1000 \\ 0.44 & Re \geq 1000 \end{cases} \quad \text{(T2-20)}$$

drag force between water and gas, water and sorbent is expressed by the symmetric model, and the drag force between powder and gas is described by the Wen−Yu model. The main governing and constitutive equations involved in the gas−liquid−solid multiphase flow model are shown in Tables 1 and 2.

2.2. Desulfurization Model. *2.2.1. Desulfurization Reaction Principles.* In this paper, we will develop a desulfurization model based on TFT and apply it to the Euler−Euler CFB-FGD process to predict SO_2 removal, the desulfurization reaction process is as follows:

(a) SO_2 in high-temperature flue gas diffuses from the main body of the gas phase to the gas−liquid interface;

(b) SO_2 enters the liquid phase from the gas−liquid interface and begins to dissolve on the surface of the liquid film;

$$SO_2(g) \Leftrightarrow SO_2(aq) \quad (1)$$

(c) Dissolved SO_2 generates H_2SO_3 in water and dissociates:

$$SO_2(aq) + H_2O(l) \Leftrightarrow H_2SO_3(aq) \quad (2)$$

https://doi.org/10.1021/acsomega.2c07658
ACS Omega 2023, 8, 5861−5876

$$H_2SO_3(aq) \Leftrightarrow HSO_3^- + H^+ \quad (3)$$

$$HSO_3^- \Leftrightarrow SO_3^{2-} + H^+ \quad (4)$$

(d) In the liquid membrane, SO_3^{2-} diffuses to the center of the liquid phase;
(e) the desulfurizer $Ca(OH)_2$ is dissolved and ionized; and
(f) ions react in water to produce desulfurization products and other products:

$$Ca(OH)_2(s) \Leftrightarrow Ca^{2+} + 2OH^- \quad (5)$$

$$Ca^{2+} + SO_3^{2-} + \frac{1}{2}H_2O(l) \Rightarrow CaSO_3\cdot\frac{1}{2}H_2O(s) \quad (6)$$

To sum up, the total reaction formula of this reaction is as follows:

$$SO_2(g) + Ca(OH)_2(s) \Rightarrow CaSO_3\cdot\frac{1}{2}H_2O(s) + \frac{1}{2}H_2O(l) \quad (7)$$

The desulfurization efficiency is defined as follows:

$$\varphi_{SO_2} = \frac{C_{in,SO_2} - C_{out,SO_2}}{C_{in,SO_2}} \quad (8)$$

2.2.2. Model Assumptions. Based on TFT, the following assumptions were made in the desulfurization process by Cai et al.:[31]

(1) Assume that only one particle is wrapped inside the liquid film.
(2) Both droplets and desulfurizer particles are spherical.
(3) The TFT is based on the process without considering the effect of the reaction rate.
(4) The reaction is instantaneous, the reaction takes place only within the liquid film, the reactants cannot coexist within the liquid film, and the reaction occurs on only one face of the liquid film.
(5) The evaporation of the liquid follows Raoul's law and does not take into account the phase change.

2.2.3. Heat and Mass Transfer Model. The desulfurization process is a process in which heat and mass transfer coexist.

The heat transfer model:

$$\frac{\partial}{\partial t}(\alpha_i\rho_i H_i) + \nabla(\alpha_i\rho_i H_i v_i) = \nabla(k_{eff}\nabla T) + h_{gs}(T_g - T_s) + h_{gl}(T_g - T_l) + h_{ls}(T_l - T_s) + S_i \quad (9)$$

where H is the total enthalpy, k_{eff} is the thermal conductivity, h is the heat transfer coefficient, the heat transfer coefficient is related to the Nusselt number of the particle phase, the heat transfer coefficient in this paper is chosen from the Gunn model, S is the source term, the heat of chemical reaction is neglected because the heat released by the chemical reaction is very little, and no source term.

The mass transfer model:

According to the above assumptions, the desulfurization model is as follows:

The mass transfer flux of SO_2 in the gas film is expressed as follows:

$$N_{SO_2} = k_g^{SO_2}(P_{SO_2} - P_{SO_{2,i}}) \quad (10)$$

In the equation, where $k_g^{SO_2}$ is the mass transfer coefficient (m/s) of SO_2 in the gas film, P_{SO_2} and $P_{SO_{2,i}}$ are the partial pressures of SO_2 (kPa) in the main body of the gas phase and on the surface of the gas film, respectively.

Considering that the chemical reaction has a transient enhancement, the mass transfer flux of SO_2 within the liquid membrane is as follows:

$$N_{SO_2} = k_l^{SO_2} E C_{SO_{2,i}} \quad (11)$$

where $k_l^{SO_2}$ is the mass transfer coefficient (m/s) of SO_2 in the liquid film, $C_{SO_{2,i}}$ is the concentration of SO_2 on the surface of the liquid film (kmol/m^3); E is the enhancement factor, denoted as the following:

$$E = \frac{D_{Ca(OH)_{2,l}} C_{Ca(OH)_{2,i}}}{D_{SO_{2,l}} C_{SO_{2,i}}} \quad (12)$$

where $D_{Ca(OH)_{2,l}}$ and $D_{SO_{2,l}}$ are the diffusion coefficients (m/s) of $Ca(OH)_2$ and SO_2 in the liquid film, respectively.

The relationship between the SO_2 concentration $C_{SO_{2,i}}$ on the surface of the liquid film and the partial pressure P_{SO_2} of SO_2 in the main body of the gas phase is given by the following:

$$C_{SO_{2,i}} = HP_{SO_2} \quad (13)$$

where H is the Henry coefficient (kmol/m^3 kPa).

The mass transfer flux of $Ca(OH)_2$ is related to its saturation concentration, as shown in the following equation:

$$N_{Ca(OH)_2} = k_s(C^*_{Ca(OH)_2} - C_{Ca(OH)_{2,i}}) \quad (14)$$

where k_s is the mass transfer coefficient of Ca $(OH)_2$ (m/s); $C^*_{Ca(OH)_2}$ is the saturated concentration of Ca $(OH)_2$ in the liquid membrane (kmol/m^3); and $C_{Ca(OH)_{2,i}}$ is the concentration of $Ca(OH)_2$ in the liquid membrane (kmol/m^3).

Coupling (10)−(14), ignoring the gas film mass transfer process, simplifies to obtain the following:

$$N_{SO_2} = \frac{C_{SO_{2,i}} + \omega C^*_{Ca(OH)_2}}{\frac{1}{k_l^{SO_2}} + \frac{\beta d_d^2}{k_s d_s^2}} \quad (15)$$

In the equation, d_d and d_s are the diameters of droplets and $Ca(OH)_2$ particles, respectively (m); ω is the ratio of the diffusion coefficients of $Ca(OH)_2$ and SO_2 in the liquid film, which can be expressed as follows:

$$\omega = \frac{D_{Ca(OH)_{2,l}}}{D_{SO_{2,l}}} \quad (16)$$

The liquid film mass transfer coefficient can be expressed as follows:

$$k_l^{SO_2} = \frac{D_{SO_{2,l}}}{\xi} \quad (17)$$

where ξ is the liquid film thickness (m). The liquid film thickness ξ can be determined from the mass fraction Y_{H_2O} of the droplets, and the expression of Y_{H_2O} is as follows:

https://doi.org/10.1021/acsomega.2c07658
ACS Omega 2023, 8, 5861−5876

$$\xi = \begin{cases} 0.5d_s(Y_{H_2O} + 1)^{-1/3} & Y_{H_2O} > 0.05 \\ 0.5d_s(Y_{H_2O} + 1)^{-1/3} + 400 \\ \quad (0.05 - Y_{H_2O})^4 & Y_{H_2O} \le 0.05 \end{cases} \tag{18}$$

$Ca(OH)_2$ particle dissolution mass transfer coefficient can be defined as follows:

$$k_s = \frac{D_{Ca(OH)_{2,l}}}{\xi_s} \tag{19}$$

where ξ_s is the thickness of $Ca(OH)_2$ dissolved liquid film (m), calculated as follows:

$$\xi_s = \frac{d_s}{Sh} = \frac{d_s}{2} \tag{20}$$

The diffusion coefficients of $Ca(OH)_2$ and SO_2 in the liquid film can be expressed as follows:

$$D_{Ca(OH)_{2,l}} = 3.954 \times 10^{-9} \times T_d \times \exp\left(\frac{-2046}{T_d}\right) \tag{21}$$

$$D_{SO_{2,l}} = T_d \times \exp\left(-19.896 - \frac{1800}{T_d}\right) \tag{22}$$

2.3. Geometry Model. The semi-dry CFB desulfurization process is a complex multiphase reaction system, and Figure 1 depicts this desulfurization process flow. The process is not only technically mature but also recycles the desulfurizer, which saves the amount of desulfurizer to a large extent. As shown in Figure 2, the structure diagram and grid division of the conventional fluidized bed are shown. In the semi-dry CFB-FGD, for a conventional fluidized bed, the mutual transfer between the gas and solid phases gradually decreases as the bed height increases, and solid particles form aggregates or accumulate in the bed,[29] leading to a decrease in the desulfurization effect. Therefore, many jets were opened at the bottom and middle symmetrical sides of the bed to form a BMJFB and MMJFB, as shown in Figure 3. In the BMJFB, the jet width is 5 mm and the number is 3. In the MMJFB, the jet width is 30 mm and the number is 3. The multi-jet structure disturbs the flow of particles in the bed, intensifies the transfer process of gas and solid phases, accelerates the fluidization of particles, and improves the efficiency of the subsequent desulfurization work.

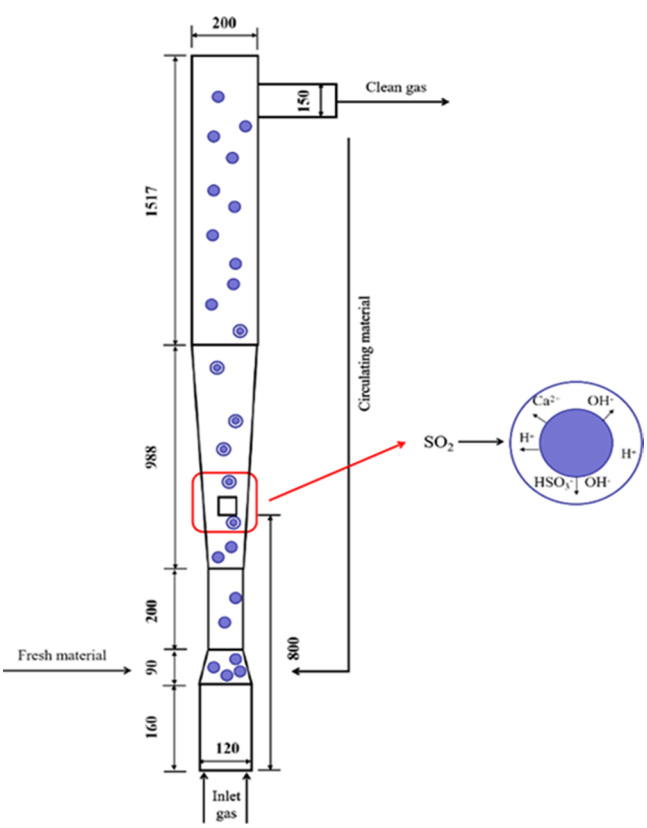

Figure 1. Principle of semi-dry circulating desulfurization in a fluidized bed.

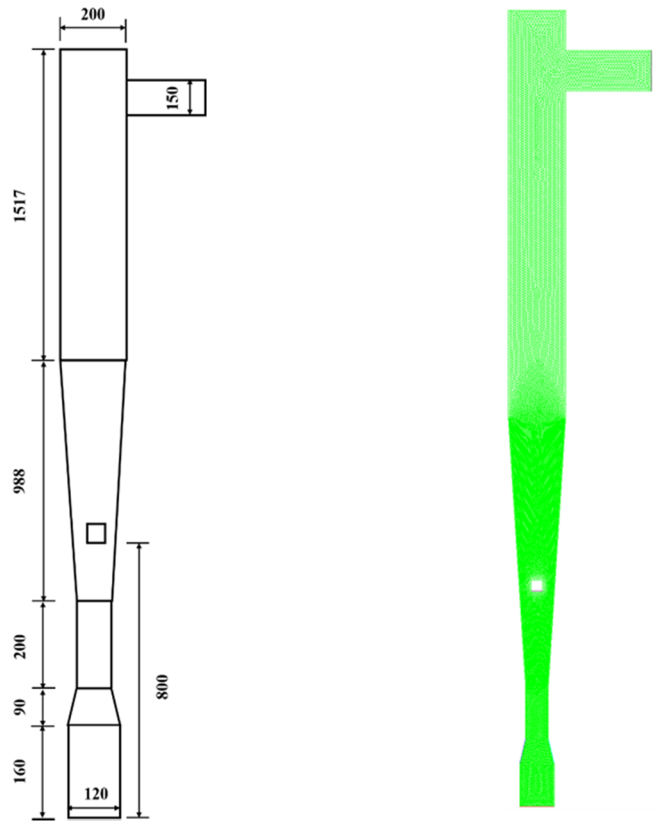

Figure 2. Structure diagram and grid division of the conventional fluidized bed (unit: mm).

3. RESULTS AND DISCUSSION

In this section, the multiphase model will be used to simulate the multiphase flow process and desulfurization process in two new MJFBs. Multi-jet is added at the bottom and middle of the fluidized bed to form an auxiliary multi-jet structure, so as to realize the fluidization state of side jets at the bottom inlet and middle inlet, thereby interfering with the flow of solid particles in the bed. Using the CFD numerical simulation method, the parameters of particle concentration distribution, particle volume fraction, particle velocity distribution, and water volume fraction were obtained and compared with the simulation results of the conventional fluidized bed. Table 3 lists the setting of simulation parameter values of the conventional fluidized bed and MJFB. Table 4 lists the calculation settings in the simulation.

https://doi.org/10.1021/acsomega.2c07658
ACS Omega 2023, 8, 5861−5876

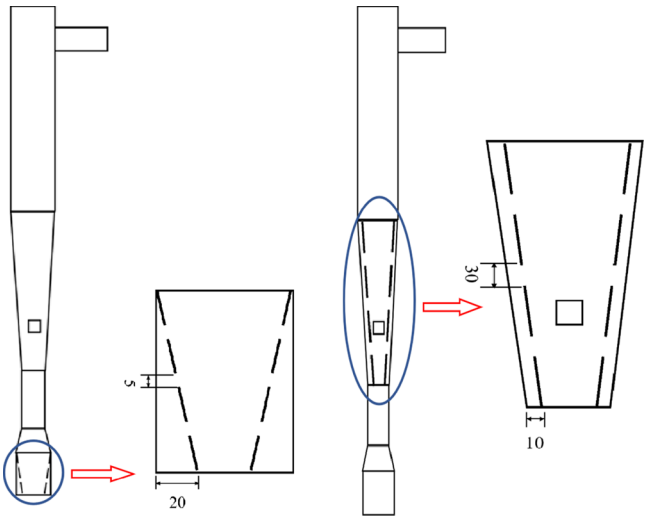

Figure 3. Structural diagram of bottom and middle MJFBs and enlarged view of local multi-jet (unit: mm).

3.1. Grid Independent Verification. The grid size has a great influence on the calculation results. Therefore, before the calculation simulation, the independence of the grid number of the MJFB calculation model is tested and analyzed. The grid independence of conventional fluidized beds has been verified by Cai et al.[31] Therefore, it is necessary to verify the mesh independence of the two new models. The number of calculation grids of the BMJFB is set to 36,692, 41,492, 42,718, and 47,719, respectively, and the number of calculation grids of the MMJFB is set to 38,400, 43,060, 47,388, and 52,654, respectively. The grid independence of the calculation model is analyzed. Figure 4 shows the maximum particle velocity at the axis center under different grid numbers when the bed height H = 1.5 m. When the number of grids is greater than 42,718 and 47,388, respectively, the maximum particle velocity in the axial center of the bottom and middle MJFB is basically unchanged, and the numerical simulation meets the requirements of grid independence. In the following calculation, the number of grids in the BMJFB is 42,718, and the number of grids in the MMJFB is 47,388.

3.2. Model Verification. The experimental desulfurization efficiency was obtained by Wang[30] et al. The desulfurization efficiency obtained by simulating the conventional fluidized bed with the same model is compared with the experimental value, as shown in Figure 5. The average desulfurization efficiency of the numerical simulation is 58.5%, which is very close to the experimental value (64.6%) with a relative error of 9.4%. The

Table 4. Calculation Settings in the Simulation

options		set value
solver		2D, double precision, pressure-based, transient, planar
multiphase model		Eulerian
viscous model		standard $k-\omega$ model, dispersed
drag coefficient		Gidaspow model
frictional stress		Schaeffer model
restitution coefficient		0.9
time step		0.0001 s
solution methods	momentum	first-order upwind
	volume fraction	
	turbulent kinetic energy	
	specific dissipation rate	
solution controls	momentum	0.7
	volume fraction	0.5
	turbulent kinetic energy	0.8
	specific dissipation rate	0.8

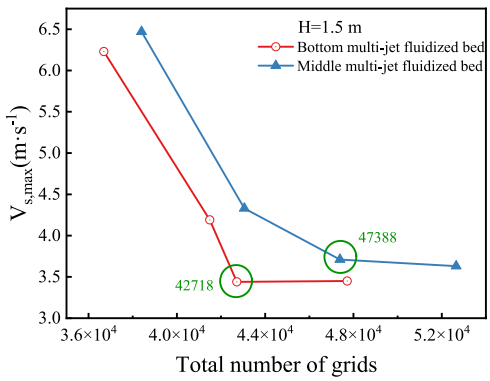

Figure 4. Grid independence verification.

Table 3. Setting of Simulation Parameter Values

simulation parameter	conventional fluidized bed	MJFBs
inlet of gas	gas phase density is 1.182 kg/m^3, gas phase viscosity is 1.8×10^{-5} Pa s, inlet gas velocity is 8 m/s, turbulent intensity is 5%, the turbulent viscosity ratio is 10, and inlet gas temperature T = 373.15 K	gas phase density is 1.182 kg/m^3, gas phase viscosity is 1.8×10^{-5} Pa s, inlet gas velocity is 8 m/s, turbulent intensity is 5%, the turbulent viscosity ratio is 10, and inlet gas temperature T = 373.15 K
	the mass fraction of each component of the inlet gas is H_2O = 0, SO_2 = 0.001354, and O_2 = 0.23264.	the mass fraction of each component of the inlet gas is H_2O = 0, SO_2 = 0.001354, O_2 = 0.23264.
spray water inlet	the volume flow rate of spray water is 2.5 L/h (the velocity of spray water is 5.529×10^{-4} m/s), spray water temperature T = 293.15 K, and volume fraction of water is 1.	the volume flow rate of spray water is 2.5 L/h (the velocity of spray water is 5.529×10^{-4} m/s), spray water temperature T = 293.15 K, and volume fraction of water is 1.
fresh material	velocity is 3.73e-05 m/s, temperature T = 293.15 K, volume fraction is 0.2, density is 2240 kg/m^3, and the particle diameter is 0.1 mm.	velocity is 3.73e-05 m/s, temperature T = 293.15 K, volume fraction is 0.2, density is 2240 kg/m^3, and the particle diameter is 0.1 mm.
circulating material	velocity is 0.01 m/s, temperature T = 353.15 K, volume fraction is 0.5, density is 2240 kg/m^3, and the particle diameter is 0.1 mm.	velocity is 0.01 m/s, temperature T = 353.15 K, volume fraction is 0.5, density is 2240 kg/m^3, and the particle diameter is 0.1 mm.
out	pressure outlet	pressure outlet
number of multi-jet		3
width of the multi-jet		BMJFB is 5 mm. MMJFB is 30 mm.

https://doi.org/10.1021/acsomega.2c07658
ACS Omega 2023, 8, 5861−5876

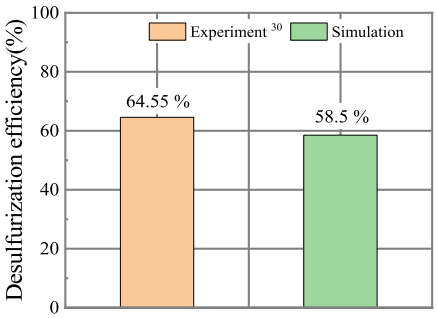

Figure 5. Comparison of desulfurization efficiency between the simulation and experiment.

relative error may be related to the instability of the fluidized bed, model simplification, etc. Therefore, the mathematical model used in this study is considered to be reliable.

3.3. Multiphase Flow. With the addition of flue gas, desulfurizer, and water, the desulfurization reaction process is a multiphase flow process involving fluid flow, heat and mass transfer of gas−liquid−solid three phases. The multiphase fluid models were used to simulate the process.

3.3.1. Different Structural Models. Figure 6 shows the variation of particle concentration distribution with time in the

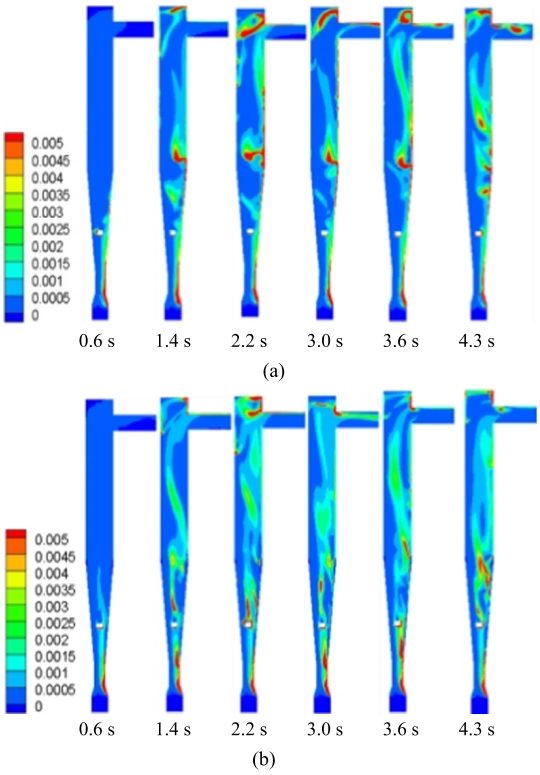

Figure 6. Distribution of particle concentration with time in two MJFBs: (a) BMJFB. (b) MMJFB.

BMJFB and MMJFB. In Figure 6, it can be seen that the particle distribution in the bed shows a skewed state and accumulates on one side of the bed because the mass flow rate of the circulating material is larger than that of the fresh material. According to the contour of particle concentration distribution, it can be found that the particle concentration distribution in the two MJFBs is basically the same with the extension of the calculation time, and the particle flow field distribution shows a circulating flow state, indicating that the gas−liquid−solid flow in the bed has reached a stable state.

Figure 7 shows the comparison of the particle volume fraction between two MJFBs and conventional fluidized beds under

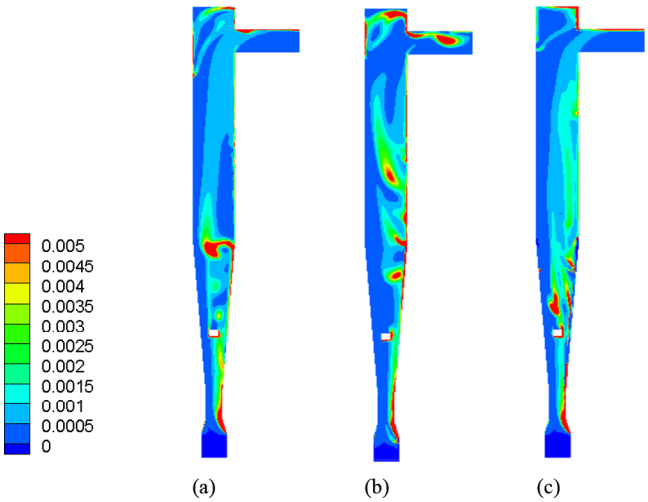

Figure 7. Different model solid particle volume fraction: (a) Conventional fluidized bed. (b) BMJFB. (c) MMJFB.

stable spouting fluidization conditions. It can be seen from the comparison that compared with the conventional fluidized bed, the bottom and middle MJFBs accelerate the fluidization of solid particles, promote the full mixing of gas−liquid−solid three phases, and is conducive to improving the uniformity of particle distribution in the bed. Compared with the multi-jet structure at the bottom, the fluidization of particles in the MMJFB is more obvious. In addition to the accumulation of a few particles due to the wall effect and the liquid inlet structure, the solid particles in the whole bed have higher distribution uniformity (DU). However, the intensification of the bottom multi-jet structure on particle agglomeration is not very obvious, and there are still some particle agglomeration phenomena.

Figure 8 shows the comparison of particle volume fraction distribution of the three models under different bed heights. It can be seen from the comparison that the particle volume fraction distribution of MJFB is generally lower than that of the conventional fluidized bed. Because the flow rate of circulating material is much larger than that of fresh material, the volume fraction of solid particles at a negative radial distance is larger than that at positive radial distance. With the increase of bed height, the fluidization effect of the BMJFB on solid particles is lower than that of the MMJFB. In addition, the kinetic energy of the gas decreases with the increase of the bed height, coupled with the wall effect, resulting in the accumulation of solid particles in the bed wall when the bed height is high.

Figure 9 shows the contours of water volume fraction distribution in a conventional fluidized bed, bottom and middle MJFBs. Compared with the traditional fluidized bed, the addition of a multi-jet structure can enhance the radial DU of water in the bed and promote the full mixing of gas−liquid−solid three phases. Comparing the two models with multi-jet in the bottom and middle of the bed, it is found that there is water accumulation in the BMJFB, so the fluidization effect of adding multi-jet in the middle of the bed is more obvious. To sum up, for the intensification effect of gas−liquid−solid mixing in the

https://doi.org/10.1021/acsomega.2c07658
ACS Omega 2023, 8, 5861−5876

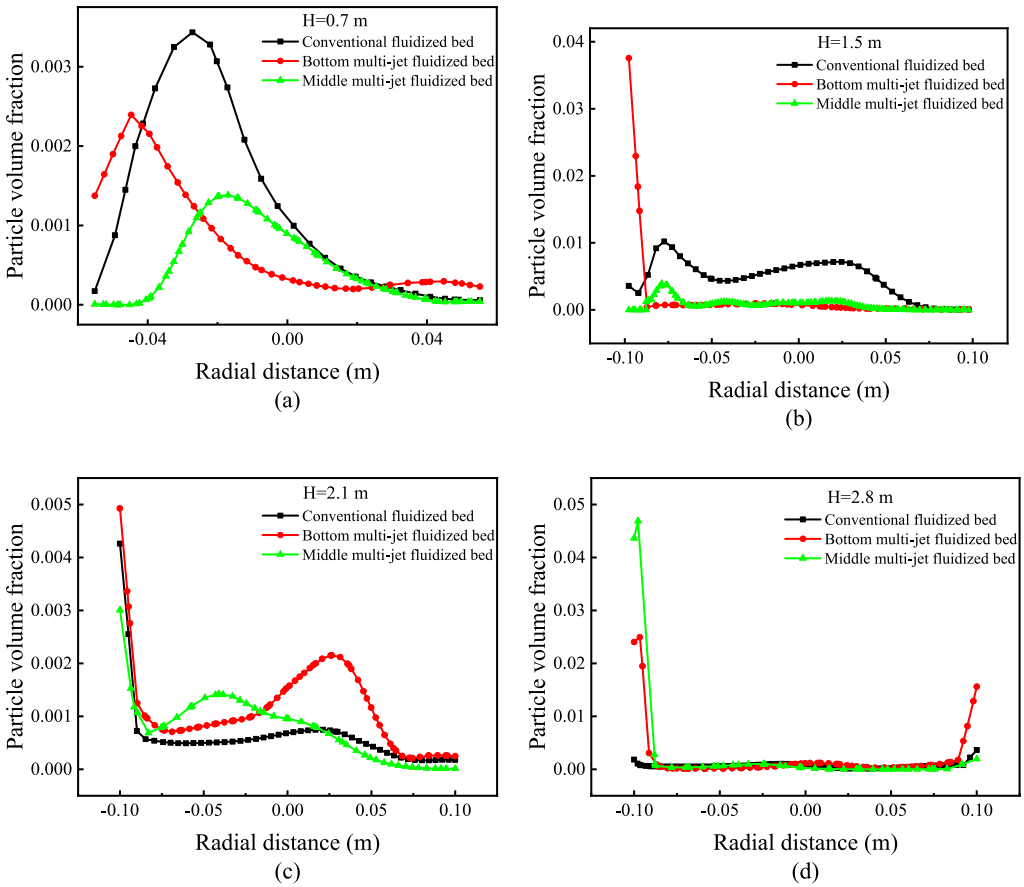

Figure 8. Particle volume fraction distribution of three models with different bed heights: (a) $H = 0.7$ m. (b) $H = 1.5$ m. (c) $H = 2.1$ m. (d) $H = 2.8$ m.

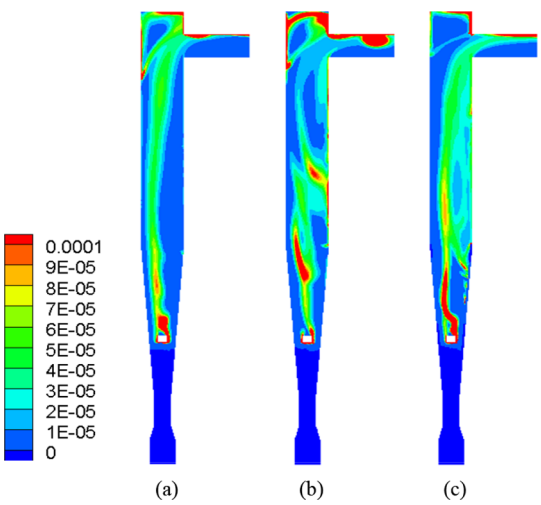

Figure 9. Different model water volume fraction: (a) Conventional fluidized bed. (b) BMJFB. (c) MMJFB.

bed, the MMJFB is larger than the BMJFB. Therefore, the MMJFB will be selected for further research.

3.3.2. Effect of Water Spray Volume Flow Rates. According to Cai's studies, the water spray volume flow rates have a great impact on the multiphase flow process, thus affecting the subsequent desulfurization process. The multiphase flow and desulfurization process in the MMJFB were studied with different water spray volume flow rates. The simulated working conditions are shown in Table 5.

Table 5. Simulated Condition

serial number	number of multi-jet	width of multi-jet (mm)	water spray volume flow rates (L/h)
1	3	30	2.0
2	3	30	2.5
3	3	30	3.0
4	3	30	3.5

Figure 10 shows the effect of different water spray volume flow rates on the concentration distribution of solid particles in the MMJFB. With the increase of water spray volume flow rates, the distribution of solid particles in the bed is more uniform, the aggregation of solid particles near the water inlet is significantly reduced, and the axial distribution of solid particles in the bed is increased.

Figure 11 shows the effect of water spray volume flow rates on the radial distribution of the solid particle volume fraction in the MMJFB at different bed heights. It can be seen in Figure 11 that when the bed height is 0.7 m, the water spray volume flow rate increases, but the particle volume fraction does not change significantly. This is because the water inlet is at the bed height of 0.8 m. With the increase of the bed height, the distribution of the solid particle volume fraction in the radial distance is promoted. On the whole, when the water spray volume flow rate is 3.5 L/h, the radial distribution of the solid particle volume fraction at different bed heights is smaller, and the distribution of solid particles in the bed is more uniform.

There are generally five evaluation indexes for the uniformity of flow field velocity distribution: relative standard deviation (CV), uniformity index (γv), based on area weighted average

https://doi.org/10.1021/acsomega.2c07658
ACS Omega 2023, 8, 5861−5876

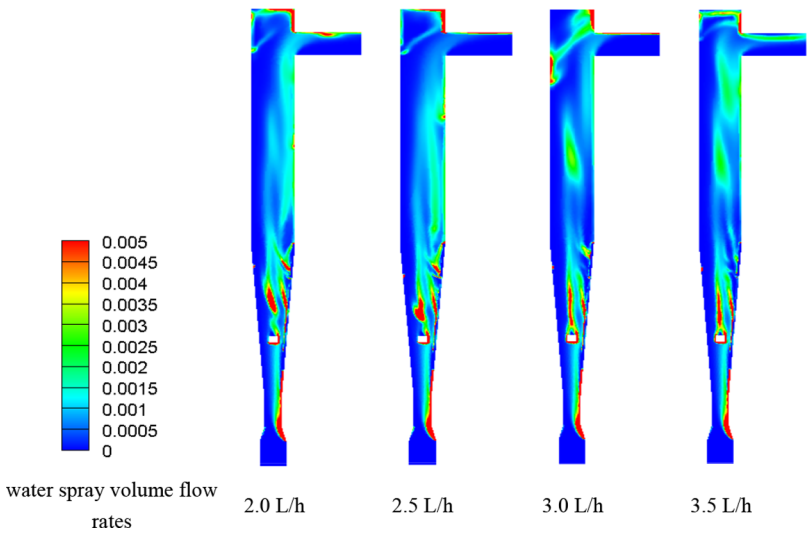

Figure 10. Effect of water spray volume flow rates on the particle concentration distribution in the MMJFB.

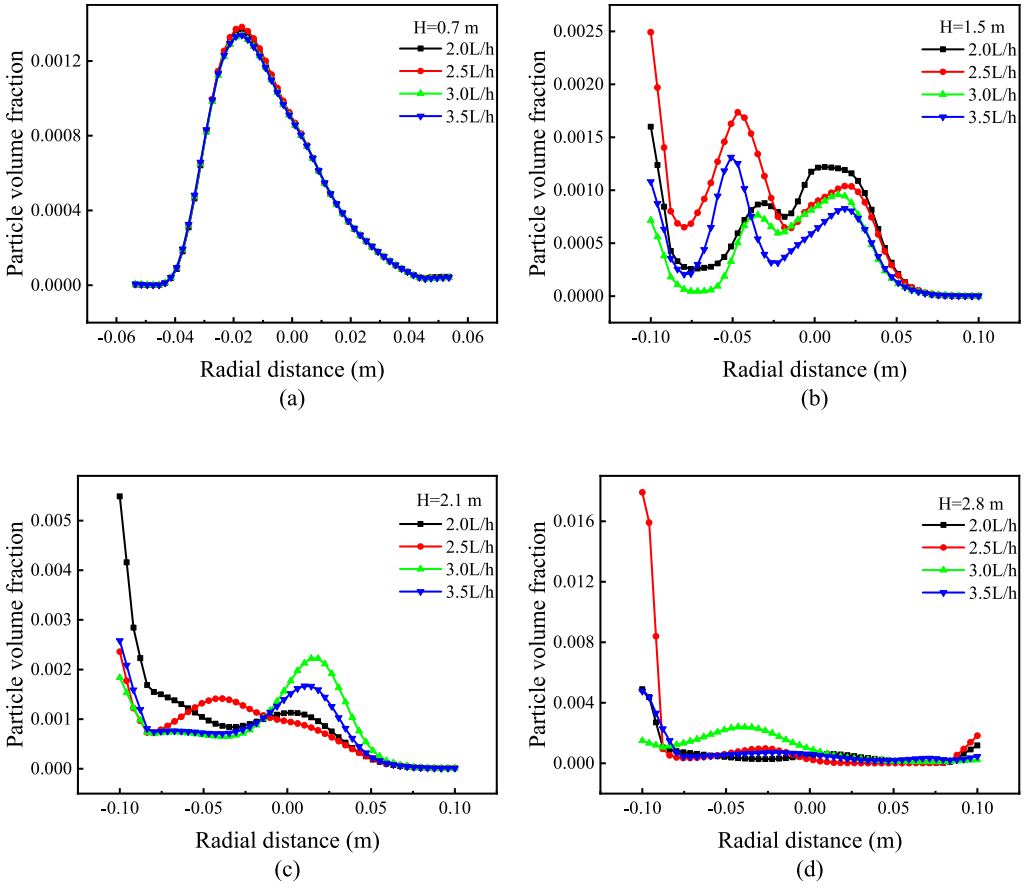

Figure 11. Effect of water spray volume flow rates on particle volume fraction distribution in the MMJFB at different bed heights: (a) $H = 0.7$ m. (b) $H = 1.5$ m. (c) $H = 2.1$ m. (d) $H = 2.8$ m.

speed and mass-weighted average speed λ, Christensen uniformity coefficient, and DU coefficient.[39] Here, the relative standard deviation (CV) is used as the evaluation index of flow field velocity DU, and the influence of different water spray volume flow rates on the flow field uniformity of the MMJFB model is analyzed. CV is a measure of relative variation. It is a dimensionless value, which can be used to compare the overall dispersion with significantly different average values and also to compare the enhancement of flow field uniformity:

$$\mathrm{CV} = (S/V) \times 100\% \tag{23}$$

$$S = \sqrt{\frac{1}{n-1}\sum_{j=1}^{n}(V_j - V)^2} \tag{24}$$

where S is the standard deviation, V_j is the velocity value of the j sampling point, $\overline{V}$ is the average speed of all sampling points, and n is the number of sampling points. The uniformity of the flow

https://doi.org/10.1021/acsomega.2c07658
ACS Omega 2023, 8, 5861−5876

field is evaluated by comparing the CV values under different working conditions. The smaller the CV value is, the higher the uniformity of the flow field is.

Table 6 and Figure 12 show the comparison of CV values of the MMJFB with different water spray volume flow rates at different bed heights. It can be seen that at 0.7 m, the water spray volume flow rate has little effect on the relative standard deviation of particle velocity, while at 1.5 m, the relative standard deviation of solid particles near the jet is larger. Due to the instability of gas−liquid−solid flow in the fluidized bed, at the same water spray volume flow rate, according to the average value of the relative standard deviation of different bed heights, when the water spray volume is 3.5 L/h, the CV value is the smallest, that is, the uniformity of particle velocity flow field is the highest, and the uniformity of gas−liquid−solid three-phase mixing is the best.

Table 6. Comparison of Calculation Results of Relative Standard Deviation CV Values (%) of Particle Velocity in Different Water Spray Volume Flow Rates

bed height	water spray volume flow rates			
	2.0 L/h	2.5 L/h	3.0 L/h	3.5 L/h
0.7 m	56.7	56.5	56.2	56.4
1.5 m	77.4	77.8	77.8	77.5
2.1 m	63.1	64.4	56.1	59.2
2.8 m	53.7	46.3	70.9	43.4
average	62.7	61.3	65.3	59.1

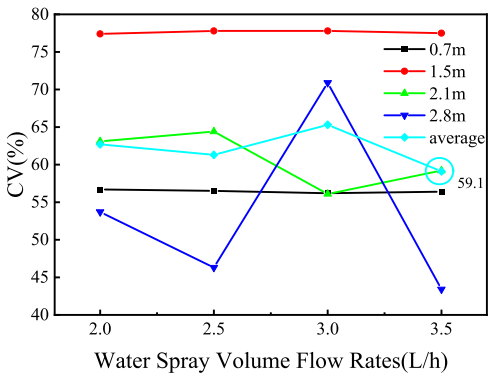

Figure 12. Comparison of CV values of the MMJFB with different water spray volume flow rates at different bed heights.

3.3.3. Effect of the Side Jet Number. In order to further understand the effect of key design parameters (number of jets) on the multiphase flow process in the MMJFB and investigate the effect of different number of jets on the multiphase flow in the MMJFB, for the convenience of analysis, a dimensionless parameter δ/D_i is set as the ratio of the jet width to the gas inlet diameter, where δ is the jet width and D_i is the gas inlet diameter. Given a jet width value $\delta/D_i = 0.167$ (the jet width is 20 mm and the gas inlet diameter is 120 mm).

The working conditions of the MMJFB simulated in this section are shown in Table 7, and other boundary conditions and parameter settings are the same as before.

Figure 13 shows the particle concentration distribution of multiphase flow in the MMJFB with 3, 4, and 5 jets when $\delta/D_i = 0.167$ (jet width 20 mm and gas inlet diameter 120 mm). It can be seen in Figure 13 that when the number of jets is three, there is a particle agglomeration near the water inlet. This is due to the fact that with the entry of water spray, dry solid particles become slurry when encountering water. In addition, the number of jets is small, and the gas fails to fully mix with solid particles, resulting in clusters of solid particles at the water inlet. When the number of jets is three, the gas velocity decreases with the increase of bed height, and solid particles accumulate when the bed is high. When the number of jets is five, due to the increase of the number of jets and the phenomenon of bias flow, the particles in the bed form a circular flow, and the solid particles in the bed rise along one side with the gas and then fall along the other side, and a large number of particles gather at the bed wall. When the number of jets is four, the solid particles in the bed are evenly dispersed as a whole, except that there are solid particles gathering at the inlet of the circulating material.

Table 7. Simulated Condition

serial number	number of multi-jet	width of multi-jet (mm)
1	3	20
2	4	20
3	5	20

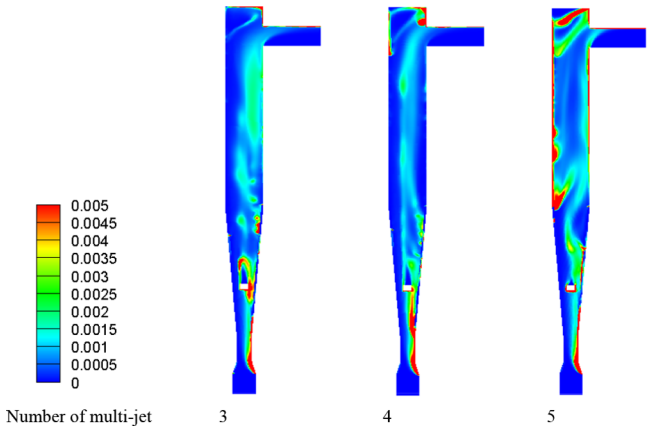

Figure 13. Effect of the jet number on the particle concentration distribution in the MMJFB.

Figure 14 shows the effect of the jet number on particle volume fraction distribution in the MMJFB at different bed heights. According to Figure 14, when the number of jets is four, there is a large volume fraction of solid particles at the height of 0.7 m of the bed. The reason is also mentioned earlier because the water spray inlet is at the height of 0.8 m of the bed, the dry solid particles gather into clusters when encountering humidified flue gas, and the solid particles are in a biased flow state in the fluidized bed, so this phenomenon will occur. With the increase of bed height, the radial distribution of solid particles is gradually uniform, but when the number of jets is five, the distribution of solid particles on both sides of the fluidized bed gathers with the increase of bed height because the solid particles in the bed show circular flow. According to Figures 13 and 14, when the number of jets is four, the solid particles in the bed are evenly distributed, showing the best particle distribution.

Figure 15 shows the effect of the number of jets on the particle velocity distribution in an MMJFB at different bed heights. When the bed height is low, the growth trend of solid particle velocity in fluidized beds with a different number of jets is the same. When the bed height increases, the increase of the number of jets will make the particle velocity distribution in the bed disordered. When the bed is 2.8 m, because this is the outlet of particles, the radial particle velocity trend here changes. On the whole, when the number of jets is four, the effect of improving

https://doi.org/10.1021/acsomega.2c07658
ACS Omega 2023, 8, 5861−5876

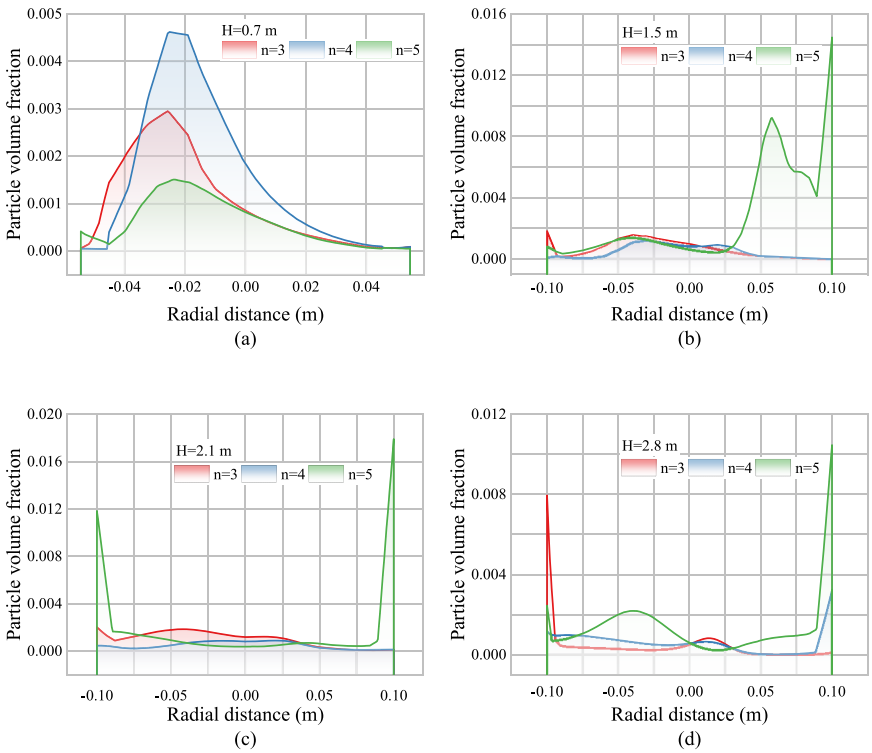

Figure 14. Effect of the jet number on particle volume fraction distribution in the MMJFB at different bed heights: (a) $H = 0.7$ m. (b) $H = 1.5$ m. (c) $H = 2.1$ m. (d) $H = 2.8$ m.

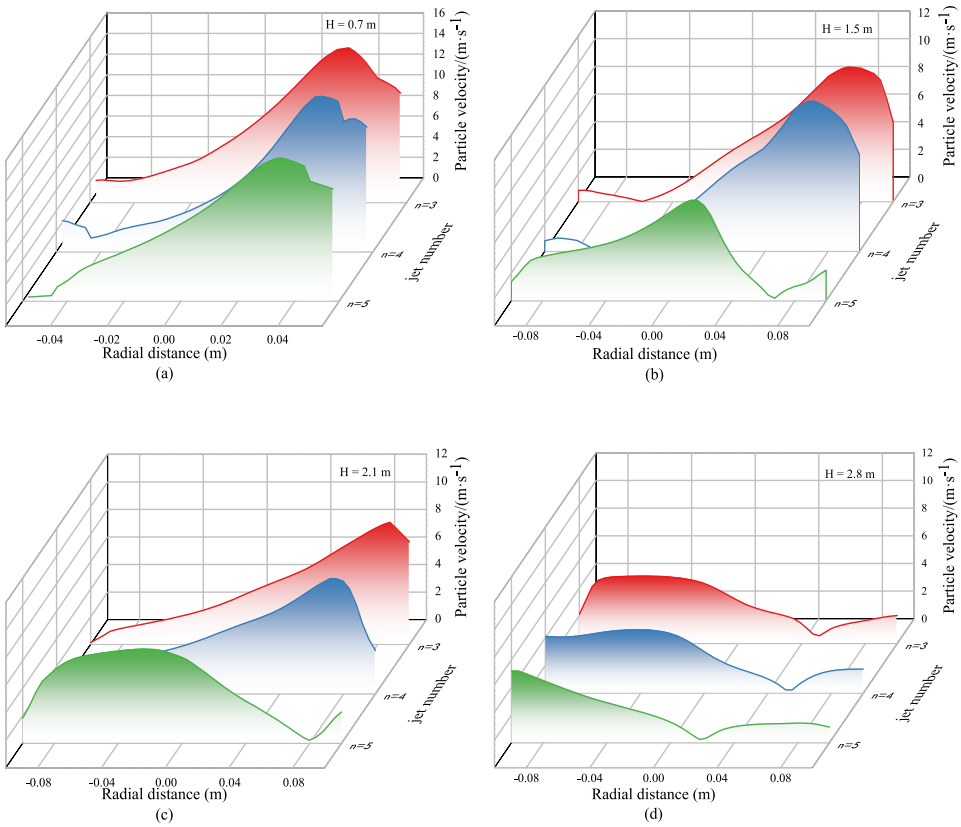

Figure 15. Effect of the jet number on particle velocity distribution in the MMJFB at different bed heights: (a) $H = 0.7$ m. (b) $H = 1.5$ m. (c) $H = 2.1$ m. (d) $H = 2.8$ m.

the movement speed of solid particles in the bed is the most obvious. Especially at the bed height of 1.5 m. Comprehensive Figures 13−15 show that when the number of jets is four, the overall particle volume distribution, velocity distribution, and

https://doi.org/10.1021/acsomega.2c07658
ACS Omega 2023, 8, 5861−5876

gas turbulent kinetic energy distribution in the MMJFB reach the optimal state.

3.3.4. Effect of Jet Width. With a certain number of jets, the effect of jet width on multiphase flow in the MMJFB is further studied. The number of jets is set to 4, and the gas inlet diameter of the MMJFB is 120 mm, and δ/D_i is 0.167, 0.25, and 0.333, respectively (the jet width is designed to be 20, 30, and 40 mm, respectively). The operating conditions of the MMJFB simulated in this section are shown in Table 8.

Table 8. Simulated Condition

serial number	number of multi-jet	width of multi-jet (mm)
1	4	20
2	4	30
3	4	40

Figure 16 shows the effect of different jet widths on the solid particle concentration distribution in the MMJFB when the number of jets is four. It can be seen in Figure 16 that although the radial distribution of solid particles in the bed is favored as the jet width increases, there are a large number of particles gathered in the inner wall of the bed, which is due to the increase in jet width, coupled with the high gas velocity at the flue gas inlet, resulting in a circular flow trend of solid particles in the bed. There is also a fluidized bed wall on the particle wall effect, so the particle distribution in the bed is not uniform. When the jet width is 20 mm, the particles in the bed are dispersed more uniformly, although there are still solid particles gathered near the inlet, as mentioned before, this is due to the mass flow rate of circulating materials is greater than that of fresh materials, resulting in a partial flow state of particles in the bed. Overall, when the jet width is 20 mm, the gas−liquid−solid phase distribution in the bed is uniform.

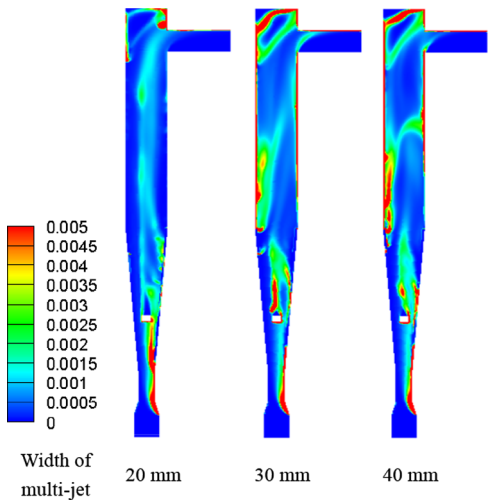

Figure 16. Effect of jet width on the particle concentration distribution in the MMJFB.

Figure 17 shows the effect of jet width on the radial distribution of the particle volume fraction in the MMJFB with different bed heights. It can be seen in Figure 17 that the particle distribution in the bed shows a nonregular variation with the increase of the open slit width, which may be related to the characteristics of the fluidized bed itself. Combined with Figure 16, it can be seen that the fluidized bed with a jet width of 20 mm has a nonuniform distribution of solid particles in the bed in the radial direction with some particle aggregation when the bed height is low (H = 0.7 m). However, with the increase of bed height, the particle distribution in the whole bed is gradually uniform, but there is still particle accumulation in the inner wall of the bed when the jet width is 30 mm and 40 mm. In Figures 16 and 17, it can be seen that when the jet width is 20 mm, the gas−liquid−solid phase mixing is more uniform and the overall state reaches the optimal state.

Figure 18 shows the effect of jet width on the radial distribution of particle velocity in the MMJFB with different bed heights. Since the position of the added jet is in the middle of the fluidized bed, the effect of jet width on the radial distribution of particle velocity is small when the bed height is low (H = 0.7 mm), and the overall particle radial velocity is larger for a jet width of 20 mm when the bed height increases, indicating that the best effect on the intensification of solid particle velocity in the radial distribution is achieved for a jet width of 20 mm. According to the comprehensive analysis in Figures 16−18, the gas−liquid−solid three-phase mixture in the MMJFB reaches the optimal state when the jet width is 20 mm.

3.4. Desulfurization Process. The multiphase flow processes under different models and different boundary conditions of the MMJFB were studied and analyzed in the previous section. In this section, based on what is described in the previous section, the desulfurization reaction process under the optimal model structure (jet number equals four and jet width equals 20 mm) and working conditions (the water spray volume flow rate is 3.5 L/h) of the MMJFB is investigated, and the desulfurization efficiency is analyzed and calculated for all previous model structures and working conditions of the MMJFB. This is a desulfurization model based on TFT, which is applied to the desulfurization process of the Euler−Euler CFB-FGD and can effectively predict the removal of sulfur dioxide in practical applications.

Figure 19 illustrates the contours of SO_2 mass fraction in the MMJFB with time. The mass fractions of the initial inlet gas components are H_2O = 0, O_2 = 0.23264, and SO_2 = 0.001354. Figure 19a depicts the mass fraction contours of SO_2 at the optimal model structure. Figure 19b reflects the mass fraction contours of SO_2 at the optimal working conditions when the model structure is constant. According to Figure 19, it is found that the SO_2 content in the MMJFB gradually decreases with the desulfurization reaction as time goes on. Among them, the solid particles present a partial flow state as mentioned before, which leads to the left−right imbalance of the in-bed desulfurization reaction as well, which indicates that the desulfurization region is mainly the right side of the MMJFB.

The contours of the desulfurization product generation rate and the desulfurization product volume fraction of the MMJFB are presented in Figure 20. Figure 20a shows the contours of the desulfurization product generation rate and the desulfurization product volume fraction for the best model structure, where the desulfurization reaction rate on the right side of the bed is larger than that on the left side due to the bias flow condition because of the mass flow rate of the circulating material being larger than that of the fresh material, and thus the desulfurization product generation rate and volume fraction are larger on the right side compared to the left side. In addition, due to the higher inlet flue gas velocity, most of the solid desulfurizer particles are carried to the upper layer of the fluidized bed, and therefore, the desulfurization reaction is mainly concentrated in the upper region of the fluidized bed. Figure 20b depicts the contours of

https://doi.org/10.1021/acsomega.2c07658
ACS Omega 2023, 8, 5861−5876

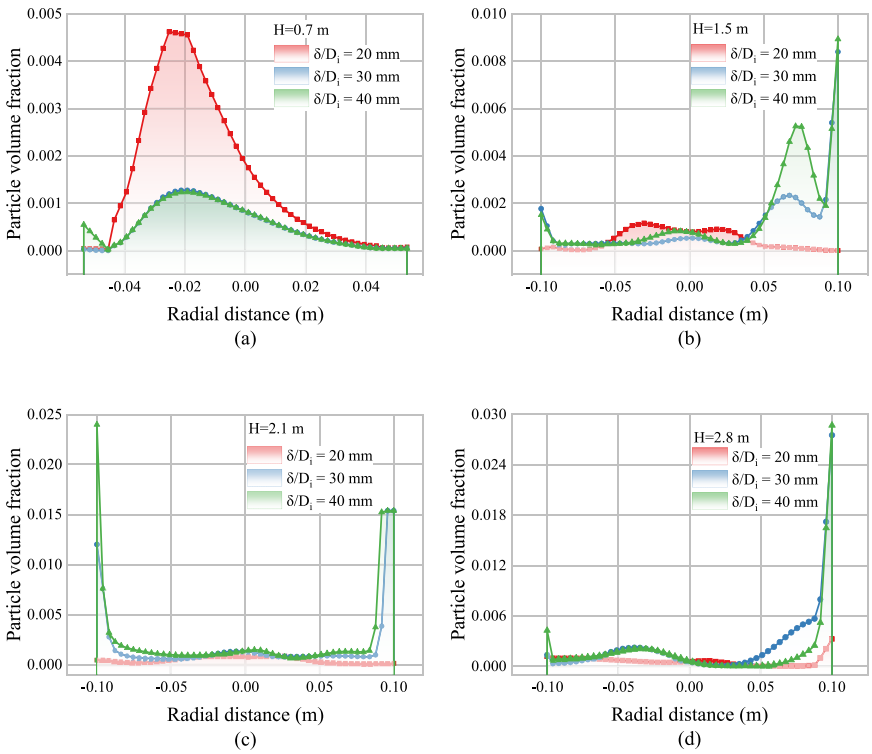

Figure 17. Effect of jet width on particle volume fraction distribution in the MMJFB at different bed heights: (a) $H = 0.7$ m. (b) $H = 1.5$ m. (c) $H = 2.1$ m. (d) $H = 2.8$ m.

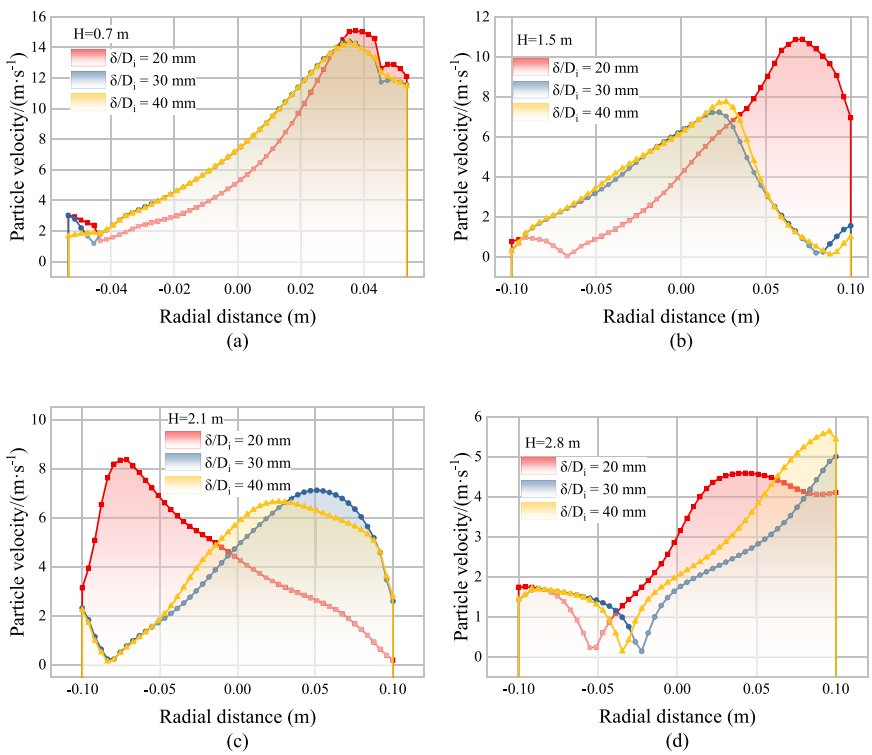

Figure 18. Effect of jet width on particle velocity distribution in the MMJFB at different bed heights: (a) $H = 0.7$ m. (b) $H = 1.5$ m. (c) $H = 2.1$ m. (d) $H = 2.8$ m.

the desulfurization product generation rate and the volume fraction of the desulfurization product at a water spray volume flow rate of 3.5 L/h. The desulfurization pattern under this condition is similar to the multi-jet structure described above, and the desulfurization area is mainly concentrated in the right and upper parts of the bed. Comparing Figure 20a,b, it is found that the addition of a multi-jet structure is more favorable to the desulfurization reaction process than changing the water flow rate.

https://doi.org/10.1021/acsomega.2c07658
ACS Omega 2023, 8, 5861−5876

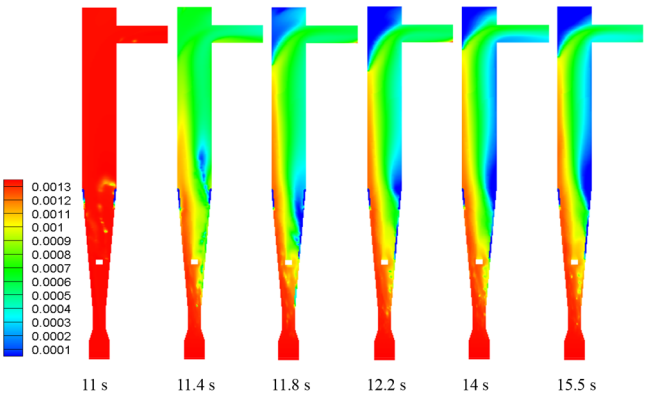

(a) SO_2 mass fraction (jet width is 20 mm, the number of jets is 4)

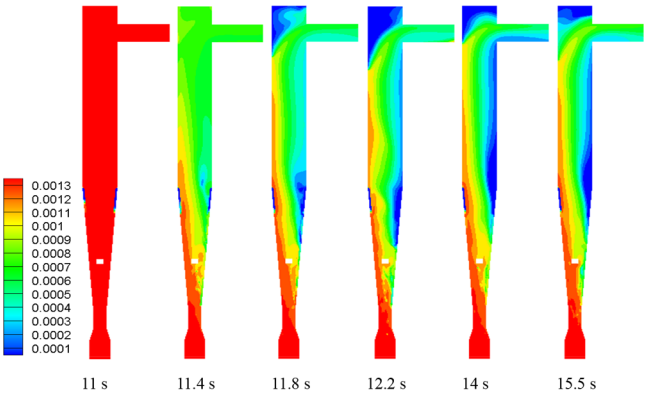

(b) SO_2 mass fraction (water spray volume flow rate of 3.5 L/h)

Figure 19. (a, b) Contours of SO_2 mass fraction with time.

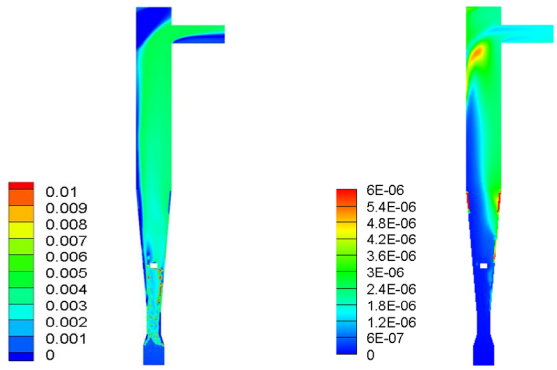

(1) Desulfurization product generation rate (2) Volume fraction of desulfurization product

(a) Desulfurization product generation rate and volume fraction for the optimal model structure

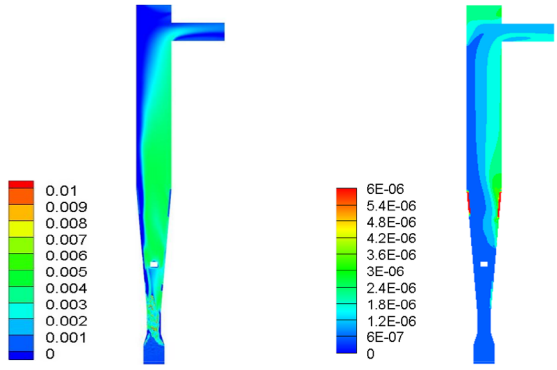

(1) Desulfurization product generation rate (2) Volume fraction of desulfurization product

(b) Desulfurization product generation rate and volume fraction for optimal boundary conditions

Figure 20. (a and b) Distribution of the desulfurization product generation rate ($kg \cdot m^{-3} \cdot s^{-1}$) and the volume fraction of desulfurization product ($CaSO_3$).

Table 9 and Figure 21 show the effect of different factors on the desulfurization efficiency of the MMJFB. Case 0 is the desulfurization efficiency of the conventional fluidized bed. As can be seen in Table 9, the desulfurization efficiency of all other cases is higher than case 0. Cases 1−4 express the effect of the water spray volume flow rate on the desulfurization efficiency. The desulfurization efficiency increases with the increase of the water volume flow rate. When the water volume flow rate is 3.5 L/h, the desulfurization efficiency increases to 68.2%. Cases 5−7 depict the effect of the number of jets on the desulfurization efficiency. Setting the jet width at 20 mm, the maximum desulfurization efficiency is reached when the number of jets is four, which is consistent with the effect on the multiphase flow process. Cases 8−10 show the effect of jet width on the desulfurization process. With a constant number of jets set at four, the highest desulfurization efficiency is reached when the jet width is 20 mm, which indicates that keeping the number of jets constant, the variation of jet width has less effect on the desulfurization efficiency. All in all, the maximum desulfurization efficiency of 69.3% is achieved in the MMJFB when the number of jets is four and the jet width is 20 mm, which is 18.5% higher compared to the conventional fluidized bed (58.5%).

In summary, the addition of the multi-jet structure promotes the multiphase flow process and intensifies the gas−liquid−solid three-phase mixing effect, resulting in an improved desulfurization efficiency compared to the conventional model. The disadvantage is that, in order to meet the corresponding national standards, the desulfurization efficiency is not very high compared to industrial applications. One of the reasons may be that the contact time between the flue gas and desulfurizer is too short due to the excessive inlet gas velocity. In this case, the contact time between the two may be the main factor affecting the desulfurization efficiency. Therefore, the inlet gas velocity should be reduced and the desulfurization process should be further investigated.

Table 9. Effect of Different Factors on Desulfurization Effect

	dependent variable				independent variable
case	gas velocity (m/s)	width of multi-jet (mm)	number of multi-jet	water spray volume flow rates (L/h)	desulfurization efficiency (%)
0	8			2.5	58.5
1		30	3	2.0	64.7
2		30	3	2.5	66.5
3		30	3	3.0	67.7
4		30	3	3.5	68.2
5		20	3	2.5	68.9
6		20	4	2.5	69.3
7		20	5	2.5	67.5
8		20	4	2.5	69.3
9		30	4	2.5	67.4
10		40	4	2.5	63.1

4. CONCLUSIONS

In this study, the MJFB is used to study the semi-dry FGD, and the CFD simulation is used to evaluate the multiphase flow process, and it was compared with the conventional fluidized bed. The main conclusions are as follows:

https://doi.org/10.1021/acsomega.2c07658
ACS Omega 2023, 8, 5861−5876

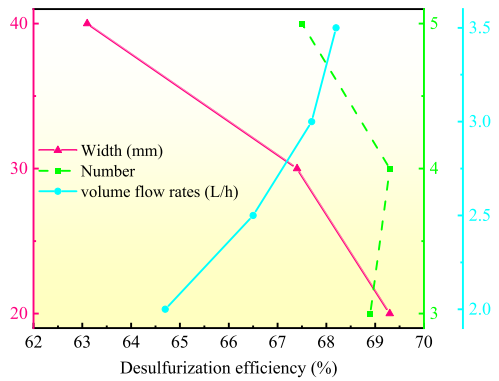

Figure 21. Effect of different factors on desulfurization efficiency.

(1) Compared with the conventional fluidized bed, the MMJFB has a stronger intensification effect on gas−liquid−solid mixing than the BMJFB.
(2) When the volume flow rate of water spray is 3.5 L/h, the gas−liquid−solid three-phase dispersion in the MMJFB is more uniform and the desulfurization efficiency is improved with a value of about 68.2%.
(3) The addition of a multi-jet structure increases the radial velocity of solid particles, improves the uniformity of the particle flow field, and intensifies the desulfurization effect. When the number of jets is four and the jet width is 20 mm, the gas−liquid−solid three-phase mixing state is optimal, and the desulfurization efficiency of the MMJFB equals 69.3%, which is 18.5% higher than that of the conventional fluidized bed (58.5%).

AUTHOR INFORMATION

Corresponding Author

Feng Wu − *School of Chemical Engineering, Northwest University, Xi'an 710069, China;* orcid.org/0000-0002-8943-4926; Phone: +86-15309202861; Email: wufeng@nwu.edu.cn

Authors

Shuai Wang − *School of Chemical Engineering, Northwest University, Xi'an 710069, China*

Bei bei Di − *School of Chemical Engineering, Northwest University, Xi'an 710069, China*

Yuan Yan − *School of Chemical Engineering, Northwest University, Xi'an 710069, China*

Yang chao Tang − *Luoyang Jianguang Special Equipment Co., Ltd., Luoyang 471003, China*

Complete contact information is available at: https://pubs.acs.org/10.1021/acsomega.2c07658

Notes

The authors declare no competing financial interest.

ACKNOWLEDGMENTS

This work was supported by the National Natural Science Foundation of China (Grant no. 22178286) and the Shaanxi Qinchuangyuan "scientist and engineer" team construction project (Grant no. 2022KXJ-041).

NOMENCLATURE

d_s particle diameter [mm]
g_0 radial distribution coefficient [dimensionless]
I unit tensor [dimensionless]
k turbulent kinetic energy [m^2/s^2]
Re Reynolds number [dimensionless]
β_{gs} gas-particle drag coefficient [dimensionless]
ε turbulence dissipation [m^2/s^3]
v velocity vector [m/s]
θ granular temperature [m^2/s^2]
ρ density [kg/m^3]
μ shear viscosity [kg/(m s)]
τ stress tensor [n/m]
γ inclination angle of the swirl blade [°]

REFERENCES

(1) Li, B. L.; Haneklaus, N. The role of clean energy, fossil fuel consumption and trade openness for carbon neutrality in China. *Energy Rep.* **2022**, *8*, 1090−1098.
(2) Saleh, T. A. Global trends in technologies and nanomaterials for removal of sulfur organic compounds: Clean energy and green environment. *J. Mol. Liq.* **2022**, *359*, No. 119340.
(3) Jr-Tsung, H. Sulfur dioxide (SO_2) emissions and government spending on environmental protection in China-Evidence from spatial econometric analysis. *J. Cleaner Prod.* **2018**, *175*, 431−441.
(4) García-Labiano, F.; Rufas, A.; de Diego, L. F.; de las Obras-Loscertales, M.; Gayán, P.; Abad, A.; Adánez, J. Calcium-based sorbents behaviors during sulphation at oxy-fuel fluidized bed combustion conditions. *Fuel* **2011**, *90*, 3100−3108.
(5) Tao, M.; Jin, B. S.; Zhong, W. Q.; Yang, Y. P.; Xiao, R. Numerical and experimental study on flue gas desulfurization in the underfeed circulating spouted bed. *Chem. Eng. J.* **2010**, *159*, 149−158.
(6) Fakhari, M. A.; Rahimi, A.; Hatamipour, M. S.; Fozooni, A. Non-isothermal modeling of simultaneous CO_2 and SO_2 removal in a semi-dry spouted bed reactor. *Process. Saf. Environ. Prot.* **2015**, *98*, 342−353.
(7) Fakhari, M. A.; Rahimi, A.; Hatamipour, M. S.; Fozooni, A. Experimental study of simultaneous removal of CO_2 and SO_2 in a spouted bed reactor. *Can. J. Chem. Eng.* **2017**, *95*, 1150−1155.
(8) Li, X. K.; Han, J. R.; Liu, Y.; Dou, Z. H.; Zhang, T. A. Summary of research progress on industrial flue gas desulfurization technology. *Sep. Purif. Technol.* **2022**, *281*, No. 119849.
(9) Wang, N. H.; Zhang, X. P. Effect of Humidification Water on Semi-Dry Flue Gas Desulfurization. *Procedia Environ. Sci.* **2011**, *11*, 1023−1028.
(10) Du, C. C.; Yi, H. H.; Tang, X. L.; Zhao, S. Z.; Gao, F. Y.; Yu, Q. J.; Yang, Z. Y.; Yang, K.; Xie, X. Z.; Ma, Y. Q. Desulfurization and denitrification experiments in SDA system: A new high-efficient semi-dry process by $NaClO_2$. *Sep. Purif. Technol.* **2020**, *230*, No. 115873.
(11) Cui, G. W.; Sun, M. Y.; Li, Y. J.; Guo, Q. K. A Brief Analysis of Coal Desulfurization before Combustion. *Adv. Mater. Res.* **2012**, *512-515*, 2477−2481.
(12) Baek, C.; Seo, J.; Choi, M.; Cho, J.; Ahn, J.; Cho, J. Utilization of CFBC Fly Ash as a Binder to Produce In-Furnace Desulfurization Sorbent. *Sustainability* **2018**, *10*, 4854−4854.
(13) Yuan, C.; Su, S. Q.; Xu, R. G.; Liang, S. W.; Cheng, H. R.; Yao, Z. B.; Jiang, L. X.; Wang, Z. W. Effect of wet flue gas desulfurization on the concentrations and component profiles of condensable particulate matter from ultralow emission coal-fired power plants. *Atmos. Pollut. Res.* **2022**, *13*, No. 101376.
(14) Ma, K. H.; Deng, J. Y.; Ma, P. S.; Sun, C. F.; Zhou, Q.; Xu, J. A novel plant-internal route of recycling sulfur from the flue gas desulfurization (FGD) ash through sintering process: From lab-scale principles to industrial practices. *J. Environ. Chem. Eng.* **2022**, *10*, No. 106957.
(15) Hou, B.; Qi, H. Y.; You, C. F.; Xu, X. C. Dry Desulfurization in a circulating fluidized bed (CFB) with chain reactions at moderate temperatures. *Energy Fuels* **2005**, *19*, 73−78.
(16) Zhang, J.; You, C. F.; Zhao, S. W.; Chen, C. H.; Qi, H. Y. Characteristics and Reactivity of Rapidly Hydrated Sorbent for Semidry Flue Gas Desulfurization. *Environ. Sci. Technol.* **2008**, *42*, 1705−1710.

(17) Shen, Z. G.; Chen, X.; Tong, M.; Guo, S. P.; Ni, M. J.; Lu, J. Studies on magnesium-based wet flue gas desulfurization process with oxidation inhibition of the byproduct. *Fuel* **2013**, *105*, 578−584.
(18) Ma, X. X.; Kaneko, T.; Guo, Q. M.; Xu, G. W.; Kato, K. Removal of SO_2 from flue gas using a new semi-dry flue gas desulfurization process with a powder-particle spouted bed. *Can. J. Chem. Eng.* **1999**, *77*, 356−362.
(19) Ma, X. X.; Kaneko, T.; Tashimo, T.; Yoshida, T.; Kato, K. Use of limestone for SO_2 removal from flue gas in the semidry FGD process with a powder-particle spouted bed. *Chem. Eng. Sci.* **2000**, *55*, 4643−4652.
(20) Ma, X. X.; Kaneko, T.; Xu, G.; Kato, K. Effect of gas components on removal of SO_2 from flue gas in the semidry FGD process with a powder-particle spouted bed. *Fuel* **2001**, *80*, 673−680.
(21) Zhang, Q.; Gui, K. T. A novel semidry flue gas desulfurization process with the magnetically fluidized bed reactor. *J. Hazard. Mater.* **2009**, *168*, 1341−1345.
(22) Zhang, Q.; Gui, K. T.; Wang, X. Effects of magnetic fields on improving mass transfer in flue gas desulfurization using a fluidized bed. *Heat Mass Transfer* **2016**, *52*, 331−336.
(23) Li, Y. R.; Qi, H. Y.; You, C. F.; Yang, L. Z. Comprehensive sulfation model verified for T-T sorbent clusters during flue gas desulfurization at moderate temperatures. *Fuel* **2010**, *89*, 2081−2087.
(24) Zhang, J.; You, C. F.; Qi, H. Y.; Chen, C. H.; Xu, X. C. Effect of Solids Concentration Distribution on the Flue Gas Desulfurization Process. *Environ. Sci. Technol.* **2006**, *40*, 4010−4015.
(25) Zhang, J.; You, C. F.; Qi, H. Y.; Hou, B.; Chen, C. H.; Xu, X. C. Effect of Operating Parameters and Reactor Structure on Moderate Temperature Dry Desulfurization. *Environ. Sci. Technol.* **2006**, *40*, 4300−4305.
(26) Fan, B.; You, C. F.; Qi, H. Y.; Xiang, G.; Xu, X. C. Effect of Chemical and Thermodynamic Parameters on the Flue Gas Desulfurization Efficiency in a Circulating Fluidized Bed. *J. Therm. Sci.* **2001**, *10*, 285−288.
(27) Zhang, J.; You, C. F.; Chen, C. H. Effect of internal sturcture on flue gas desulfurization with rapidly hydrated sorbent in a circulating fluidized bed at moderate temperatures. *Ind. Eng. Chem. Res.* **2010**, *49*, 11464−11470.
(28) Tang, Q.; Wang, Q.; Cui, P. F.; Cao, W. W.; Hou, S. F. Numerical simulation of flue gas desulfurization characteristics in CFB with bypass ducts. *Process Saf. Environ. Prot.* **2013**, *91*, 386−390.
(29) Du, J. L.; Yue, K.; Wu, F.; Ma, X. X.; Hui, Z. Q. Numerical investigation on the water vaporization during semi dry flue gas desulfurization in a three-dimensional spouted bed. *Powder Technol.* **2021**, *384*, 471−483.
(30) Wang, X.; Li, Y. J.; Zhu, T. Y.; Jing, P. F.; Wang, J. S. Simulation of the heterogeneous semi-dry flue gas desulfurization in a pilot CFB riser using the two-fluid model. *Chem. Eng. J.* **2015**, *264*, 479−486.
(31) Cai, L.; Xu, Z. Y.; Wang, X. R.; Bai, H. C.; Han, L. C.; Zhou, Y. F. Numerical simulation and optimization of semi-dry flue gas desulfurization in a CFB based on the two-film theory using response surface methodology. *Powder Technol.* **2022**, *401*, No. 117268.
(32) Wang, S. Y.; Zhao, L. Q.; Wang, C. S.; Liu, Y. S.; Gao, J. S.; Liu, Y.; Cheng, Q. L. Numerical simulation of gas-solid flow with two fluid model in a spouted-fluid bed. *Particuology* **2014**, *14*, 109−116.
(33) Liu, X. J.; Shao, Y. J.; Zhong, W. Q.; Grace, J. R.; Epstein, N.; Jin, B. S. Prediction of minimum spouting velocity by CFD-TFM: Approach development. *Can. J. Chem. Eng.* **2013**, *91*, 1800−1808.
(34) Gidaspow, D.; Bezburuah, R.; Ding, J.*Hydrodynamics of circulating fluidized beds: Kinetic Theory Approach*. Fluidization VII, Proceedings of the Seventh Engineering Foundation Conference on Fluidization, 1992; pp 75 −82.
(35) Schaeffer, D. G. Instability in the evolution equations describing incompressible granular flow. *J. Differ. Equ.* **1987**, *66*, 19−50.
(36) Wang, S. Y.; Shao, B. L.; Liu, R.; Zhao, J.; Liu, Y.; Liu, Y. K.; Yang, S. R. Comparison of numerical simulations and experiments in conical gas-solid spouted bed. *Chin. J. Chem. Eng.* **2015**, *23*, 1579−1586.
(37) Prieur Du Plessis, J. Analytical quantification of coefficients in the Ergun equation for fluid friction in a packed bed. *Transport in Porous Media* **1994**, *16*, 189−207.
(38) Wen, C. Y. Mechanics of Fluidization. *Chem. Eng. Prog. Symp. Ser.* **1966**, *62*, 100−111.
(39) Coats, A. W.; Redfern, J. P. Kinetic Parameters from Thermogravimetric data. *Nature* **1964**, *201*, 68−69.

https://doi.org/10.1021/acsomega.2c07658
ACS Omega 2023, 8, 5861−5876